

Nanoscale

Accepted Manuscript



This is an *Accepted Manuscript*, which has been through the Royal Society of Chemistry peer review process and has been accepted for publication.

Accepted Manuscripts are published online shortly after acceptance, before technical editing, formatting and proof reading. Using this free service, authors can make their results available to the community, in citable form, before we publish the edited article. We will replace this *Accepted Manuscript* with the edited and formatted *Advance Article* as soon as it is available.

You can find more information about *Accepted Manuscripts* in the [Information for Authors](#).

Please note that technical editing may introduce minor changes to the text and/or graphics, which may alter content. The journal's standard [Terms & Conditions](#) and the [Ethical guidelines](#) still apply. In no event shall the Royal Society of Chemistry be held responsible for any errors or omissions in this *Accepted Manuscript* or any consequences arising from the use of any information it contains.



Journal Name

ARTICLE

Analysing the effect of crystal size and structure in highly efficient $\text{CH}_3\text{NH}_3\text{PbI}_3$ perovskite solar cells by spatially resolved photo- and electroluminescence imaging

Received 00th January 20xx,
Accepted 00th January 20xx

DOI: 10.1039/x0xx00000x

www.rsc.org/

S. Mastroianni^{a,b}, F. D. Heinz^a, J.-H. Im^{c,d}, W. Veurman^a, M. Padilla^a, M. C. Schubert^{a,*}, U. Würfel^{a,b,*}, M. Grätzel^{c,*}, N.-G. Park^{d,*} and A. Hinsch^a

$\text{CH}_3\text{NH}_3\text{PbI}_3$ perovskite solar cells with mesoporous TiO_2 layer and Spiro-MeOTAD as hole transport layer (HTL) with three different $\text{CH}_3\text{NH}_3\text{I}$ concentrations (0.032 M, 0.044 M and 0.063 M) were investigated. Strong variations in crystal size and morphology resulting in diversified cell efficiencies (9.2%, 16.9% and 12.3%, respectively) were observed. The physical origin of this behaviour was analysed by detailed characterization combining current-voltage curves with photo- and electroluminescence (PL and EL) imaging as well as light beam induced current measurements (LBIC). It was found that the most efficient cell shows the highest luminescence and the lowest efficient cell is most strongly limited by non-radiative recombination. Crystal size, morphology and distribution in the capping layer and in the porous scaffold strongly affect the non-radiative recombination. Moreover, the very non-uniform crystal structure with multiple facets, as evidenced by SEM images of the 0.032 M device, suggests the creation of a large number of grain boundaries and crystal dislocations. These defects give rise to increased trap-assisted non-radiative recombination as is confirmed by high-resolution μ -PL images. The different imaging techniques used in this study prove to be well-suited to spatially investigate and thus correlate the crystal morphology of the perovskite layer with the electrical and radiative properties of the solar cells and thus with their performance.

Introduction

The hybrid organic–inorganic halide perovskite solar cell (PSC) is nowadays revealing a great potential as low-cost and high-performance photovoltaic device. This new PV technology demonstrated at the end 2014 a certified 20.1% efficiency¹ after three important pioneer works on the perovskite sensitized liquid junction solar cells in 2009 and 2011 and a long-term durable solid state perovskite solar cell in 2012^{2–4}. The large versatility of the perovskite material, which can be based e.g. on $\text{CH}_3\text{NH}_3\text{PbI}_3$, $\text{CH}_3\text{NH}_3\text{PbI}_{3-x}\text{Cl}_x$ or on lead-free $\text{CH}_3\text{NH}_3\text{SnI}_3$ compounds, also contributes to the great interest attracted^{5–10}. Furthermore, the variety of deposition methods and cell fabrication techniques using mesoporous scaffolds or planar structures^{11–13}, the multifunctional nature of the

perovskite complex as light emitting diode and lasing devices^{14–17}, and the efforts towards device upscaling^{18–23} are capturing the attention of diversified groups and research centres. It follows that the understanding of the physicochemical properties, as well as the electrical characteristics, are paramount for improving the device knowledge and maximizing cell's efficiency. In this sense, the efficient light-emission behavior of the perovskite light harvester, which can be investigated through electroluminescence (EL) and photoluminescence (PL) measurements, opens a wide and profitable research field⁶.

EL²⁴ and PL²⁵ directly address the fundamental principles of local radiative/non-radiative charge recombination and charge transport in solar cells^{26, 27}. Furthermore, these techniques are also recognized as a valuable and fast inspection tools for the acquisition of spatial information. In fact, EL and PL imaging are widely used to unveil the reason for reduced performance through the analysis of radiative and non-radiative pathways, which allows the determination of, e.g., recombination centers, cell defects and non-homogeneous areas with power loss^{28–30}.

The highest possible efficiency for single junction solar cells is given by the Shockley-Queisser limit³¹. Therein, the only loss mechanism is radiative recombination. As in addition it includes the assumption of full absorption of all photons with energies $h\nu \geq E_G$ (with E_G being the band gap energy of the absorber) and does not consider carrier transport, it

^a Fraunhofer Institute for Solar Energy Systems ISE, Heidenhofstr. 2, 79110 Freiburg, Germany

^b Materials Research Center FMF, University of Freiburg, Stefan-Meier-Str. 21, 79104 Freiburg, Germany

^c Laboratory for Photonics and Interfaces, Institute of Chemical Sciences and Engineering, School of Basic Sciences, Ecole Polytechnique Fédérale de Lausanne, CH-1015 Lausanne, Switzerland

^d School of Chemical Engineering and Department of Energy Science, Sungkyunkwan University, Suwon 440-746, Korea

* Corresponding author

† Electronic Supplementary Information (ESI) available: $V_{OC} - EQE_{EL}$ relation, V_{OC} vs. light intensity, I-V curves under dark, PL – EL mapping, SEM images. See DOI: 10.1039/x0xx00000x

determines the upper limit for the short-circuit current density J_{SC} , the open-circuit voltage V_{OC} and the fill factor. Real devices will suffer from additional non-radiative recombination pathways such as recombination via states with energies within the band gap (Shockley-Read Hall, SRH), Auger recombination and surface recombination³²⁻³⁵. The photo- and electroluminescence signal from a solar cell is proportional to the number of electrons and holes that recombine radiatively and, hence, it will be the higher the excess carrier density.

In PL measurements, electron-hole pairs are generated in the absorber by a light source and photons originating from radiative recombination (photoluminescence) are recorded. It was found that PL emission occurs in the perovskite itself between free electrons in the conduction band (CB) and free holes in the valence band (VB) (bimolecular free-carrier recombination)³⁶⁻³⁸. The typical PL spectrum for $\text{CH}_3\text{NH}_3\text{PbI}_3$ crystals is centered on 775 nm (1.60 eV). Electron-hole recombination also takes place with non-radiating behavior (i.e., recombination at the TiO_2 /perovskite interface, SRH recombination within the perovskite, surface recombination at the electron-hole selective contacts and excitation-density-dependent recombination following Auger mechanisms³⁸⁻⁴³). The PL intensity also depends strongly on the operating point of the device. Hence, at J_{SC} charges are prone to be efficiently separated and collected externally, whilst at V_{OC} no current flows and all photogenerated charge carriers have to recombine²⁷.

In EL measurements cells are kept in the dark and electrons and holes are injected through the respective contacts by an applied voltage through the TiO_2 and HTL into the conduction and valence band of the perovskite, respectively. It was reported that PL and EL signals have the same spectral position of the peak and thus share the same physical origin³⁶.

In this paper a detailed investigation of perovskite solar cells through PL and EL imaging is shown. Following the work done by Park et al.⁴⁴, PSCs fabricated from $\text{CH}_3\text{NH}_3\text{PbI}_3$ sensitizer with three different $\text{CH}_3\text{NH}_3\text{I}$ concentrations (methylammonium iodide, MAI = 0.032 M, 0.044 M and 0.063 M) and using spiro-MeOTAD as hole transport layer (HTL) were studied. As designed, strong variations in crystal size and structure resulting in diversified cell efficiencies were observed giving a maximum of 16.9% under simulated AM1.5G illumination ("1 sun") for 0.044 M MAI.

This paper analyses the influence of crystal size and morphology on the device performance by spatially and spectrally resolved EL and PL techniques, supported by light beam induced current measurements (LBIC). Through these techniques the variation of charge photogeneration and recombination in the devices are investigated, which we show to be closely connected with the perovskite crystal structure. High resolution μ -PL is also performed to investigate the spatial and spectral PL properties of perovskite crystals with a micrometric resolution on incomplete cells (identical setup but without HTL and Au). It emerges that the PL emission and spatial uniformity at the crystal level closely correlates with the final overall performance of the perovskite solar cell.

Results and discussion

Photoelectrode structure

The perovskite films of the as prepared incomplete cells ($\text{TCO}/\text{compact_TiO}_2/\text{mesoporous_TiO}_2/\text{perovskite}$) were characterized by SEM imaging (Figure 1) as a function of MAI concentration in the spin coated solution (0.032 M, 0.044 M and 0.063 M)⁴⁴. Crystals with wide size distribution were found for the 0.032 M sample (200 nm – 2 μm) in the crystalline capping layer above the mesoscopic TiO_2 . Moreover, large voids of perovskite material at the surface of the mesoscopic TiO_2 are visible around the vicinity of the crystals probably caused by an Ostwaldt type ripening process⁴⁵ during the crystal growth. In addition, the crystalline capping layer varies in height reaching thicknesses > 1 μm , which creates a coarse and irregular surface. These deviations are much smaller for the 0.044 M and 0.063 M samples where typical crystal sizes in the capping layer are 300-500 nm and 100-200 nm, respectively. The TiO_2 coverage in these cases is almost complete.

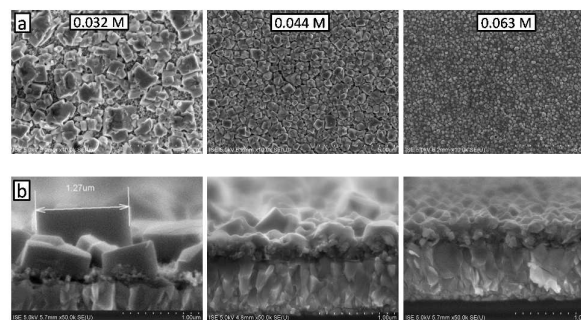


Figure 1. Surface (top view) (a) and cross section (b) SEM images for perovskite films as a function of MAI concentration (0.032 M, 0.044 M and 0.063 M). Scale bar is 5 μm for surface images and 1 μm for cross sections. A wider crystal size distribution and voids can be observed for 0.032 M MAI.

Current-voltage characteristics

Current-voltage curves and the electrical parameters of the cells close to AM1.5G illumination ("1 sun") with different MAI concentrations are plotted in Figure 2. A noteworthy ~ 100 mV lower V_{OC} is displayed for the 0.032 M cell together with a significantly reduced J_{SC} in comparison with the 0.044 M and 0.063 M samples. The 0.044 M device shows 16.9% conversion efficiency with $J_{SC}=22.8$ mA/cm^2 . The reason for this better performance is a consequence of very good light harvesting and charge carrier extraction properties, as explained in ref.⁴⁴. A small hysteresis effect, caused by charging of the devices, can be seen, which is related to the relatively fast scan speed (100 mV/s) of the measurement⁴⁴. This effect, and its extent, was described in detail by Kamat et al.⁴⁶

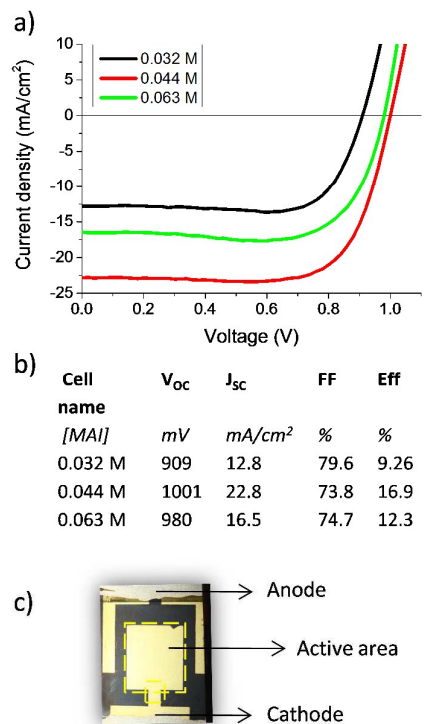


Figure 2. Current density-voltage curves (a) and main electrical parameters (b) for the perovskite solar cells with three different MAI concentrations measured close to AM1.5G illumination ("1 sun"). The scan direction was from the starting voltage of 1.2 V towards the final point at -0.1 V with 20 mV voltage step and 200 ms time interval between each step. Further experimental details for I-V measurements are described in the experimental section. Photo of the perovskite sample under analysis showing the rectangular active area of the cell inscribed into the dashed lines ($\sim 0.5 \text{ cm}^2$) (c).

PL and EL analysis

Spatially resolved PL and EL images were recorded. First the spatially averaged signals will be analysed in order to identify the physical origin of the differences in cell performance of the three typologies of cells. This will be then followed by a discussion of the spatially resolved images which enables revealing spatial inhomogeneities and their impact on the performance.

The PL intensity averaged over the active area as function of applied bias is shown in Figure 3. Here, the PL rises exponentially for all three samples but large differences in intensity can be seen, which resembles nicely both the overall efficiency and the open-circuit voltage. It can also be seen that the PL signals at short-circuit conditions ($V=0 \text{ V}$) are very comparable. However, large differences in J_{sc} values are observed (see Figure 2). In ref.⁴⁴ it is shown that the poorer light harvesting properties of the 0.032 M sample cannot be accounted for the whole difference in J_{sc} .

If the different cells have comparable PL intensities at 0 V, it can be assumed that the (average) charge carrier densities are roughly the same for the three samples. However, a much higher concentration of recombination centres in the case of 0.032 M could cause a much higher (non-radiative) recombination rate at this given charge carrier density. This in

turn would reduce the amount of charges that are extracted at the contacts. As will be shown later in detail and confirming this finding, the 0.032 M cell has a substantially lower radiative efficiency, i.e., the ratio between radiative and non-radiative recombination. It can therefore be concluded that the charge collection efficiency of this cell is lower than the one of the 0.044 M and 0.063 M samples.

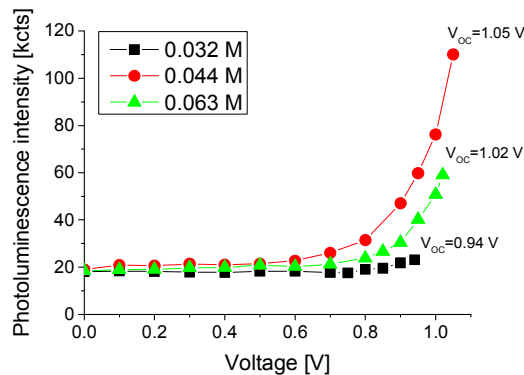


Figure 3. Averaged PL intensity values for cells with 0.032 M, 0.044 M and 0.063 M MAI concentrations as function of applied bias (from 0 V to V_{oc}). As expected, the cell with the highest V_{oc} (0.044 M) gives the highest PL emission. Lines among symbols are guide to the eye.

Figure 4a plots the current measured in the dark plotted together with the averaged EL intensity from the whole cell active area versus the applied voltage. The I-V curves comparison shows that at high voltages (1.3 V) and high currents (up to 60 mA/cm^2 for 0.032 M) no plateauing effect is observed and, thus, no limiting transport issues occur in the cells. Nevertheless, the slope of cell 0.063 M suggests higher series resistance with respect to the other two cell typologies. We further note that the 0.032 M device displays a current onset (measured at 1 mA/cm^2) about 130 mV earlier than the other two devices. These much higher dark currents well correspond to the smaller V_{oc} with respect to the 0.044 M ($\Delta V_{oc} = -90 \text{ mV}$) and 0.063 M ($\Delta V_{oc} = -70 \text{ mV}$) devices (Figure 2). We can also note from the same graph that the exponential increase of the EL signal of the cell with the lowest V_{oc} is much weaker, well in accordance with the PL data of Figure 3.

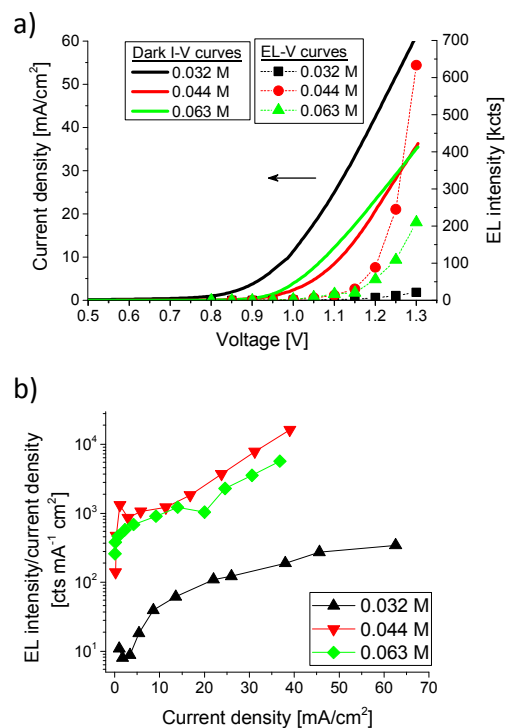


Figure 4. I-V curves measured under dark (full lines) and averaged electroluminescence intensities in the whole active area of the cells (dotted lines + symbols) as function of applied voltage (a) and normalized electroluminescence to the injected current as a function of injected current (which is a parameter related to the EL quantum yield) (b) for the MAI concentration used (0.032 M, 0.044 M and 0.063 M). Lines among symbols are guide to the eye.

In Figure 4b the EL signal divided by the injected current density is plotted vs the current density. This quantity is related to the EL yield, which expresses the emission performance of the cell. However, as the cells with the different crystal sizes will have different scattering properties, the fraction of the emitted light captured with the detector could vary slightly. Nevertheless, the light harvesting difference between cells can be approximated to be less than 15%⁴⁴ and therefore, using Kirchhoff's law of radiation, it can be expected that the difference of their emission properties is in the same range. For ease of description we refer to it as EL quantum yield or EQE_{EL} in the following. First, it can be seen that the EQE_{EL} increases for all cells with increasing current. This is a sign that the dominant recombination pathway, above all at low currents, is SRH recombination. In fact, the reaction order of the recombination pathway, i.e. the number of free charge carriers involved, is 1 for SRH recombination in contrast to radiative recombination where it is 2. With increasing current (and thus increasing voltage) the concentration of electrons and holes rises in the perovskite layer and thus the *probability* for radiative recombination increases. Similarly, an increasing PL quantum efficiency as function of excitation density was shown due to the increased ratio of radiative recombination with respect to SRH non-radiative recombination^{15, 37, 39}. How much the EQE_{EL} increases in a real device depends strongly on the overall concentration of

recombination centres. For example, it was reported that the EQE_{EL} increments by orders of magnitude for well-performing cells in contrast to devices with very high trap-assisted or SRH recombination^{36, 38} or high series resistance⁴⁷. It becomes therefore clear from Figure 4b that the 0.032 M cell is extremely limited by SRH recombination (more than one order of magnitude lower EQE_{EL} are displayed in the whole current range). In addition to this, we further observe different EQE_{EL} slopes for 0.032 M with respect to 0.044 M and 0.063 M devices at low injected currents. Intermediate states (SRH) and shunts, which behave as recombination pathways, significantly affect the EQE_{EL} values in this range. Shunts could arise due to voids of perovskite material on the TiO₂ surface and in the porous scaffold creating direct contact between TiO₂ and HTL⁴⁸⁻⁵¹. Furthermore, lower EQE_{EL} influences, in turn, the cell's V_{OC} (see ESI).

We also measured the light intensity dependence of the open-circuit voltages and the dark current-voltage curves (Figures S1 and S2 in the ESI). The very low V_{OC} values at low light intensities of the 0.032 M cell are due to a shunt which becomes clearly visible for reverse bias in the dark J-V curves of Figure S2. Nevertheless, this shunt limits the V_{OC} only for intensities < 0.1 suns where the slope of the trend is markedly steep ($k \approx 8.3 k_B T/q$, obtained by linearly fitting V_{OC} vs the illumination intensity expressed in the log scale). For intensities > 0.1 suns the slope of the curve becomes smaller but keeps being higher than for the other two cells ($k = 2.37 k_B T/q$ and $k \approx 1.07 k_B T/q$, respectively). For pure SRH recombination a slope of $2 k_B T/q$ would be expected whereas for solely radiative recombination (bimolecular recombination process of free electrons and holes) it would be $1 k_B T/q$ ⁴². This again confirms strongly our hypothesis that the 0.032 M cell is most severely limited by non-radiative SRH recombination. Hence, the overall lower EQE_{EL} for 0.032 M points to defects in the bandgap of the perovskite material which can be attributed, e.g., to crystal dislocations, untransformed PbI₂ and grain boundaries. The latter will be analysed in detail by μ -PL investigations further below.

Spatially resolved luminescence images and μ -LBIC maps

In the following, high resolution μ -LBIC maps are compared with EL and PL images in order to spatially investigate and correlate electrical and radiative properties of the perovskite solar cells and their dependence on material crystallinity. The complete set of PL images for cell 0.044 M for voltages from 0 V to V_{OC} from where the spatially averaged values were plotted in Figure 3 are shown in Figure S3 in the ESI. Accordingly, Figure S4 shows the correspondent EL images related to Figure 4. Figure 5-7 show PL images (at V=0 V and V=V_{OC}), EL images (at 0.85 V and 1.3 V) and μ -LBIC maps for the three device typologies.

Since the 532 nm excitation light for μ -LBIC measurements was incident from the glass side and the largest fraction of light is absorbed within the active layer of the devices (transmittance

at 532 nm < 10%⁴⁴), the effects of crystal scattering can be considered negligible. In fact, all the light which is scattered and thereafter absorbed, contributes to the induced current and creates only a negligible decrease of spatial resolution (the 20 μm excitation spot size is much larger than the largest crystals which are about 1-2 μm). At last, these effects are more pronounced in the red region of the spectrum (i.e., they are small at 532 nm) as described by the differences in light harvesting efficiency⁴⁴. Thus, we can assume that the diffraction effects do not yield a relevant error to the following analysis.

At first glance a generally distributed EL/PL radiation non-homogeneity appears in all cells, being largest for the 0.032 M device and smallest for 0.044 M. In particular, the former shows non-homogeneous PL and EL features (> 1 mm) caused by the non-uniform distribution in size and concentration of perovskite crystals which appear to be clustered in spots above the TiO₂ layer (also well visible in the $\mu\text{-LBIC}$ map and by naked-eye). In addition to that, a streak-pattern caused by the TiO₂ paste spin-coating process can be observed. Here hills and valleys with different mesoporous layer thicknesses are formed which alter the perovskite crystal distribution in the capping layer. As a consequence, PL and EL emission and the $\mu\text{-LBIC}$ values are significantly affected. Furthermore, bright and dark PL and EL spots (< 1 mm) arise, most probably caused by agglomerates in the spin-coating solutions and processing issues due to e.g. dust particles. As expected, the current intensity values given by $\mu\text{-LBIC}$ maps reflect the J_{sc} values (Figure 2), where the sample 0.044 M has an about 70% higher current generation at 532 nm with respect to the sample 0.032 M.

For sample 0.044 M we observe high uniformity (higher than the other two cell typologies) in the EL and PL maps (Figure 6). Interestingly here a well-defined spot in the central region of the cell area is identified, which is present at all applied bias (Figure S3 and S4). In the PL image at 0 V (Figure 6a) this spot is well visible as a bright area, which suggests that the charge carriers generated there are not efficiently transported to the electrodes and hence recombine (in part radiatively). In the corresponding EL image at 0.85 V (Figure 6d) this spot is dark, i.e., the charge carriers injected at the contacts are not transported into this area. This points strongly toward a very poorly contacted region where an agglomeration of PbI₂, and thus of perovskite crystals after the MAI dipping process, could have occurred as processing defect. The corresponding $\mu\text{-LBIC}$ map confirms this finding and shows a low photocurrent in this area (Figure 6c). In Figure 6f the voltage dependent local electroluminescence intensity is displayed for three different regions marked in Figure 6e, with the one marked with a triangle being the inactive region just described above. Its EL intensity is approximately one order of magnitude lower compared to the other two areas (identified in Figure 6e as square and circle). The latter two represent well contacted areas which, however, can be noted showing an increasing EL difference with increasing voltage. This suggests that the two dark spots inscribed into the square in Figure 6e are limited by a local series resistance causing a considerable part of the

applied voltage to drop. This effect and a similar analysis was also reported by Hinken *et al.* for silicon solar cell⁴⁷.

A similar EL and PL spatial behaviour can be observed for sample 0.063 M (Figure 7). Nevertheless, the PL image at V_{oc} shows less regions with high intensity (Figure 7b) compared to sample 0.044 M. Spots with high PL intensity at 0 V (Figure 7a) express that charge collection does not occur efficiently at these points and this is further confirmed by the EL map (at 0.85 V, Figure 7c) and $\mu\text{-LBIC}$ (Figure 7e) where low values can be detected at these positions. Under the application of high bias (Figure 7d) the distribution of brighter and darker regions changes when compared to low bias (Figure 7c). This could be due to local series resistances which may originate from the smaller crystallites and the higher number of grain boundaries. The dark I-V curves of Figure 4a also suggested a higher R_s for cell 0.063 M, which might be related to the perovskite morphology and ferroelectric polarization characteristics as confirmed by piezoresponse force microscopy (PFM) study⁵². The good spatial uniformity, the best PL and EL emission properties and the most efficient generation and extraction of charge carriers are the reasons for the high efficiency of cell 0.044 M (16.9%). Nevertheless, it is worth to note that the grooves caused by the TiO₂ spin-coating process and the other non-uniformities caused by processing defects lead to a current loss for cell 0.044 M which can be quantified by $\mu\text{-LBIC}$ to be approx. 7% at 532 nm. Similarly a V_{oc} reduction can also be expected observing the non-uniformity in the PL maps. The optimization of cell uniformity and manufacturing processes, which can be systematically analysed through PL, EL and LBIC mapping, can thus lead to a considerable improvement of cell performance.

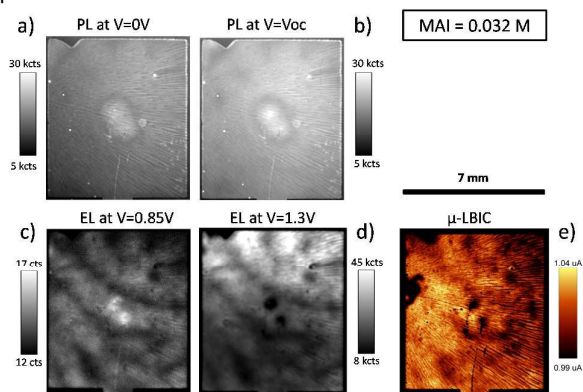


Figure 5. Photoluminescence (measured at I_{sc} ($V=0$ V) and V_{oc}) (a, b), electroluminescence imaging (applied voltage 0.85 V and 1.3 V) (c, d) and $\mu\text{-LBIC}$ map measured at 532 nm (e) for cell with 0.032 M MAI concentration. Scale bar values are set for optimized view for each image.

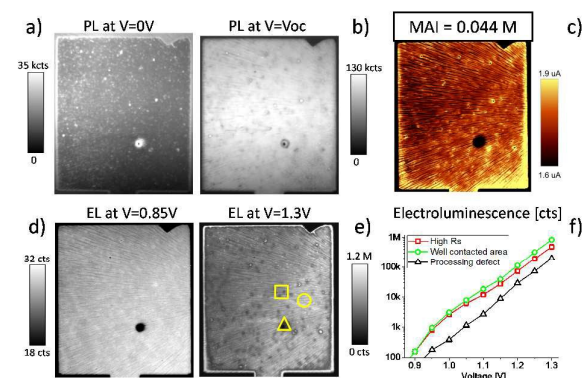


Figure 6. Photoluminescence (measured at I_{SC} ($V=0$ V) and V_{OC}) (a, b), electroluminescence imaging (applied voltage 0.85 V and 1.3 V) (d, e) and μ -LBIC map measured at 532 nm (c) for cell with 0.044 M MAI concentration. Scale bar values are set for optimized view for each image. Note that the maximum PL values at V_{OC} and EL values at 1.3 V are several times higher than those obtained from cell 0.032 M. The graph (f) shows voltage dependent local electroluminescence emission from regions illustrated in the EL image at 1.3 V (e). The two dark spots inscribed into the square are cell areas likely limited by series resistances. The black hole delimited by the triangle is a poorly contacted region because of processing defects. Cell area defined by the circle is a well contacted region with high radiative recombination.

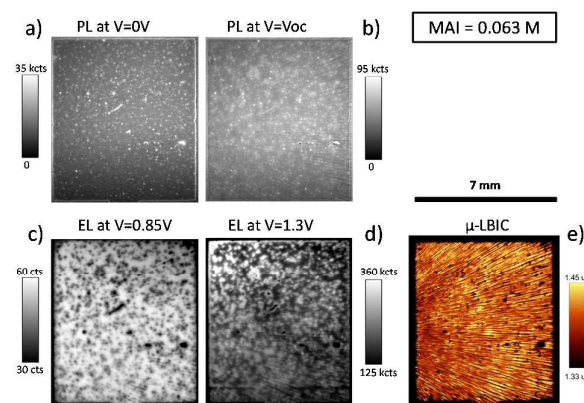


Figure 7. Photoluminescence (measured at I_{SC} ($V=0$ V) and V_{OC}) (a, b), electroluminescence imaging (applied voltage 0.85 and 1.3 V) (c, d) and μ -LBIC map (e) measured at 532 nm for cell with 0.063 M MAI concentration. Scale bar values are set for optimized view for each image. Note that the maximum PL values at V_{OC} and EL values at 1.3 V are several times higher than those obtained from cell 0.032 M (but lower than 0.044 M sample).

High resolution μ -PL imaging

Photoluminescence imaging is a useful and fast technique but it is limited by the camera resolution and can give us only averaged information about perovskite film properties. As was treated above, cell 0.032 M suffers from intermediate states and other recombination pathways (the latter originating from the non-uniform distribution of the perovskite crystals) and this accounts for the overall lower radiative efficiency and decreased performance. Nevertheless, a relevant role on this could be played by the recombination dynamics within the single crystallites⁵³. Hence, in order to investigate the single crystal emission on micrometric scale, high resolution μ -PL

imaging was performed on incomplete cells comprising a layer sequence (TCO/compact_TiO₂/mesoporous_TiO₂/perovskite). For these samples the light excited the absorber from the perovskite capping layer side. μ -PL maps overlaid with SEM images taken on the same spot are displayed in Figure 8 and show the PL intensity and spectral position of the PL peak for incomplete cells with 0.032 M and 0.044 M. We note that the PL signal recorded with 532 nm excitation light originates predominantly from the crystals of the capping layer whereas the perovskite infiltrated into the TiO₂ shows a low PL intensity. A strong inhomogeneity in both intensity and spectral position can be observed from the film processed with 0.032 M MAI. Crystals can be clearly distinguished with PL intensity ranging from 100 to 1200 cts (PL average value = 204 cts, PL distribution over the cell with standard deviation $\sigma=190$ cts), where the largest crystals show the lowest PL intensity. The μ -PL depth resolution is in the order of the crystal size. By variation of the focal plan it was ensured that the lower PL intensity detected at the large crystals is not focus induced. A precise correlation with the crystal size also follows the spectral peak which ranges from 767 nm for the smallest crystals (1.616 eV) to 774 nm for the largest (1.602 eV). Thus, an increase of crystal size leads to lower PL emission and red-shift of the peak⁴². The smaller bandgap energy for larger crystal sizes was related to a change of the lattice strain and in particular to the Pb-I bond stress by D'Innocenzo⁵⁴. A further explanation to this effect can be attributed to a higher density of trap states in large crystals, which would create a reduction of the bandgap energy and result in red-shifted PL emissions, as described by Shao et al.⁵⁵

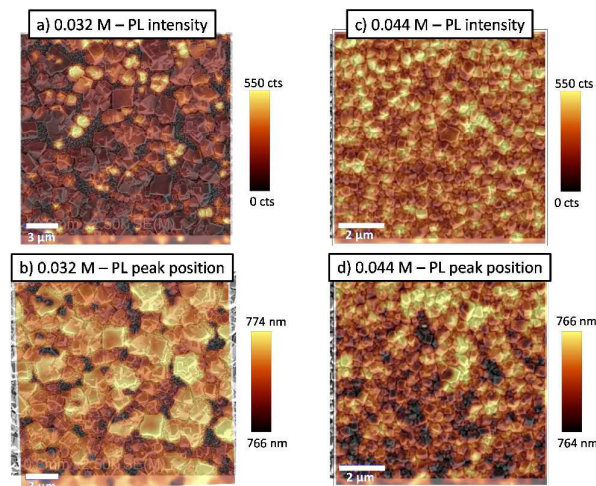


Figure 8. High resolution μ -PL imaging overlaid with SEM images acquired on the same spot, performed on incomplete cells TCO/compact_TiO₂/mesoporous_TiO₂/perovskite with 0.032 M and 0.044 M MAI concentration. μ -PL intensity (a, c) and spectral position of the PL peak (b, d) are shown. Note the different color bar in (b, d) which is 766-774 nm for sample 0.032 M and has a much smaller range (764-766 nm) for sample 0.044 M. Scale bar is 3 μ m for 0.032 M film and 2 μ m for 0.044 M.

Observing the overall data, a more uniform behaviour can be noted for samples with 0.044 M and 0.063 M MAI (not shown) with higher PL average values and lower standard deviation

($\sigma=97$ cts and 70 cts respectively). The higher standard deviation for cell 0.044 M compared to 0.063 M can be explained by the wider distribution of crystal sizes in the former case⁴⁴. The higher emission intensity for cells 0.044 M and 0.063 M compared to 0.032 M is well in agreement with what was described in the previous sections for the complete solar cells.

Hence it can be concluded that the crystal size, morphology and distribution (see high magnification SEM images, Figure S5) not only affect the overall non-radiative recombination stemming from the TiO₂/perovskite/HTL layer, but they also largely influence the recombination properties of the perovskite crystal itself.

The present findings point to an increment of recombination centres (trap states) and surface defects as the polycrystallinity of the perovskite is increased, as similarly suggested by D'Innocenzo⁵⁴. Confirming this, it was shown that the reduction of perovskite grain boundaries lead to a better cell performance in a crystallization-controlled cell fabrication process⁵⁶ and through chemical processing⁵⁷. A large presence of trap states at the interface between crystals and at their surface, where defects of the bulk crystalline symmetry occur, was also found⁴⁰. Differently, low densities of trap states were measured for large volume MAPbBr₃ and MAPbI₃ single crystals along with high charge carrier lifetime and diffusion length^{58, 59}. Hence, it can be stated that the polycrystalline structure and not defined facets of perovskite layers with non-optimal morphology (Figure S5) (present in the 0.032 M sample and less strongly in the 0.063 M sample) enhance non-radiative recombination due to trap states.

Through the above observations it can be asserted that the spatial distribution of perovskite crystals, their size distribution and morphology strongly determine the final performance of the solar cells. At low and high MAI concentrations (0.032 M and 0.063 M) these properties are not advantageous thus causing an enhanced rate of non-radiative recombination most likely due to grain boundaries, surface defects and dislocations in the perovskite crystal^{60, 61}.

Conclusions

The influence of crystal size, distribution and morphology on the performance of perovskite solar cells with three different CH₃NH₃I concentrations (0.032 M, 0.044 M and 0.063 M) was investigated by spatially and spectrally resolved electro- and photoluminescence (EL and PL) techniques supported by light beam induced current measurements (LBIC). It is found that the most efficient cell (0.044 M, 16.9% PCE) shows the highest luminescence in a wide range of applied voltages and spatial uniformity whilst the lowest efficient cell (0.032 M, 9.2% PCE) might be limited by non-radiative recombination. Analysis of the EL yield clearly shows a strongly enhanced SRH (trap states) recombination of the latter cell. Additional recombination arises due to voids of perovskite material on the TiO₂ surface and in the porous scaffold creating direct contact between TiO₂ and HTL. In contrast, the high spatial uniformity, the best PL and EL emission properties and the

most efficient generation and extraction of charge carriers are the reasons for the high efficiency and high open circuit voltage for cell 0.044 M. Morphological features seen in μ -LBIC maps have been found to be in good agreement with PL-EL imaging. High resolution μ -PL imaging was also performed in combination with SEM on perovskite films to investigate the emission behaviour at the crystal level. A strong inhomogeneity in both intensity and spectral position of the peak is observed for the perovskite film processed with 0.032 M MAI where the largest crystals show the lowest PL intensity. It is found that as the polycrystallinity of the perovskite is increased (non-uniform crystal structure with multiple facets) the PL emission is decreased. This phenomenon is ascribed to an increment of recombination centres (trap states) and surface defects due to a larger number of grain boundaries and dislocations in the perovskite crystal which is well in accordance with the results from the EL yield of the complete cell. It was shown that the PL emission and spatial uniformity at the crystal level strongly influences the electrical and radiative properties of perovskite solar cells and thus their overall performance. The combination of luminescence and current imaging techniques used in this study enables a deeper understanding of the factors limiting the performance of perovskite solar cells and open way for a systematic optimization of cell performance by achievement of optimal perovskite crystallinity and uniformity.

Experimental

Cell preparation

The solar cells have been prepared following a recently described method⁴⁴. In brief MAPbI₃ was prepared by two-step spin coating procedure. PbI₂ layer was first deposited on the mesoporous TiO₂ film deposited fluorine-doped tin oxide (FTO) conductive glass, which was followed by coating the MAI solution. MAPbI₃ layer was finally annealed at 100 °C for 5 min. Spiro-MeOTAD was spin-coated on the MAPbI₃ layer and Au was finally deposited on the spiro-MeOTAD. Incomplete cells with the three different MAI concentrations (0.032 M, 0.044 M and 0.063 M) without HTL and Au electrode were also analysed. The preparation procedures were kept identical to the complete devices.

Electrical parameters

The solar simulator used is equipped with a 1000 W xenon short arc lamp and a Keithley 2651A source meter. The light intensity was calibrated through a Si reference cell in order to give a 1 sun light intensity according to AM1.5G spectrum (class A, AM1.5G deviation < 2 %). No spectral mismatch correction was applied. For efficiency measurements, the cells were equipped with a non-reflective black mask which defined a 0.16 cm² active area (out of the total active area size of ~0.5 cm²). The scan direction was from the starting voltage of 1.2 V towards the final point at -0.1 V with 20 mV voltage step and 200 ms time interval between each step. For each typology 3-5 cells were measured giving average conversion efficiency and

standard deviation of 7.87 ± 1.31 %, 17.07 ± 0.31 %, 12.03 ± 0.58 % for 0.032 M, 0.044 M and 0.063 M, respectively. The largest standard deviation for 0.032 M devices is also representative for the stronger non-uniformity of the perovskite layer. Out of the 3-5 samples for every cell typology, one device was chosen for the complete characterization (I-V sun, I-V dark, V_{oc} vs light intensity, EL- and PL-imaging and μ -LBIC) and the corresponding results shown.

SEM

The investigation of surface and cross sections of the TiO_2 /perovskite films was carried out through a Schottky emission scanning electron microscope SEM (Hitachi, SU-70).

PL and EL setup

The experimental PL setup consists of a cooled 1 MP Silicon CCD camera, a spatially homogenous excitation light in the whole active area of the cell ($\sim 0.5 \text{ cm}^2$) with about 1.2 Sun light intensity obtained by a 2 halogen-lamp-system filtered by a 650 nm dielectric short-pass filter and an absorption band-pass filter with transmittance 500-900 nm. A power source and a stack of optical filters between the camera and the sample completed the equipment. The filter stack of the camera lens was composed by a 725 nm dielectric long-pass and an absorption long-pass with smooth edge from 720 nm to 760 nm in order to obtain a sufficient suppression of excitation light incident on the camera. Furthermore a short pass filter is put in front of the camera filter stack to suppress light above 900 nm. The operating point of the cell was changed through the power source from V_{oc} to 0 V. PL images were acquired with 50 - 100 mV voltage steps (smaller voltage steps close to V_{oc} were used to better follow the steep I-V curve behaviour in this range). For every step an equilibration time of 2 s was used. Integration time was in the range 0.1 - 0.5 s per image. The spatial resolution was about 40 μm per camera pixel. The EL setup shared the same equipment. EL measurements were performed in the dark by application of a forward bias voltage. The filter stack was removed since no filtering of excitation light was necessary. The operating point of the cell was changed from 800 mV to 1300 mV with 50 mV voltage steps while EL images were acquired. Integration time was changed as function of the operating point from 60 s to 0.5 s in order to get a high signal-to-noise ratio. It was observed that the prolonged application of high voltages during EL measurements reversibly modified the electrical characteristics of the cell. In particular, the current at a fixed high voltage was seen to decrease. A similar behaviour was also observed on the PL intensity (decrease) with light exposure. Following equilibrium conditions, the original parameters were restored within tens of seconds. A short integration time was used for PL and EL in order to minimize the device perturbation. Moreover, a recovery time of 60 s was taken between every step to avoid overheating of the device (in case of PL) and permit a complete device re-equilibration.

μ -PL and μ -LBIC scanning setup

μ -PL⁶² and μ -LBIC (Light Beam Induced Current) allow the investigation of photoluminescence and current generation with a micrometric resolution on the device. The cell is mounted on a movable stage. Excitation is done via a frequency doubled Nd:YAG laser at 532 nm, which is focused on the sample. For the large area μ -LBIC maps, an objective lens with an NA = 0.26 is used to obtain a low depth of focus. The intensity is set to 1 sun equivalent photon flux of about $7 \times 10^{17} \text{ cm}^{-2} \text{ s}^{-1}$ and spot size to 20 μm in diameter. The induced current is measured by a highly sensitive current preamplifier. Emitted PL is collected with the same lens as is used for excitation, directed towards a grating spectrometer and detected by a silicon line CCD. Doing so, the PL spectrum can be detected in the illuminated spot. By raster scanning the sample, the spatial resolution is established which is diffraction limited. For the highly resolved μ -PL maps an objective lens with numerical aperture of NA = 0.9 is used, which allows for a diffraction limited spot size of 260 nm and a corresponding spatial resolution. Typical integration times are 10 ms – 100 ms per pixel. In complete devices the laser beam was shone from the glass side, meaning that the light passes through the TCO glass till the Au back electrode of the cell. In case of properties investigation of perovskite crystals, incomplete cells were used (TCO/compact- TiO_2 /mesoporous- TiO_2 /perovskite). The high resolution μ -PL images were carried out with laser excitation from the perovskite crystal side (capping layer side). 3-5 cells for each typology were tested for generating enough statistical data for a robust investigation of μ -PL/ μ -LBIC. The resulting differences among samples of similar typology were very small compared to the differences between devices with different MAI concentrations. Cells were stored under dark and in a humidity-free environment throughout the PL-EL measurement timespan to prevent degradation effects.

Acknowledgements

This work was partially funded by the European Commission under contract no: 309194, FP7-ENERGY-2012 (Globasol project, www.globasol.eu) and the National Research Foundation of Korea (NRF) grants funded by the Ministry of Science, ICT & Future Planning (MSIP) of Korea under contracts No. NRF-2012M3A6A7054861 (Global Frontier R&D Program on Center for Multiscale Energy System).

The authors would like to thank Bernhard Michl and Laura Mundt for useful discussions, Jutta Zielonka for recording SEM images, Stephen Thomas Haag for I-V measurements.

Notes and references

1. NREL efficiency chart, 2015.
2. A. Kojima, K. Teshima, Y. Shirai and T. Miyasaka, *J Am Chem Soc*, 2009, **131**, 6050-6051.
3. J.-H. Im, C.-R. Lee, J.-W. Lee, S.-W. Park and N.-G. Park, *Nanoscale*, 2011, **3**, 4088-4093.

4. H.-S. Kim, C.-R. Lee, J.-H. Im, K.-B. Lee, T. Moehl, A. Marchioro, S.-J. Moon, R. Humphry-Baker, J.-H. Yum and J. E. Moser, *Scientific Reports*, 2012, **2**.
5. S. Colella, E. Mosconi, P. Fedeli, A. Listorti, F. Gazza, F. Orlandi, P. Ferro, T. Besagni, A. Rizzo and G. Calestani, *Chemistry of Materials*, 2013, **25**, 4613-4618.
6. H. S. Jung and N. G. Park, *Small*, 2015, **11**, 10-25.
7. E. Edri, S. Kirmayer, S. Mukhopadhyay, K. Gartsman, G. Hodes and D. Cahen, *Nat Commun*, 2014, **5**.
8. C. C. Stoumpos, C. D. Malliakas and M. G. Kanatzidis, *Inorg Chem*, 2013, **52**, 9019-9038.
9. N. K. Noel, S. D. Stranks, A. Abate, C. Wehrenfennig, S. Guarnera, A.-A. Haghighirad, A. Sadhanala, G. E. Eperon, S. K. Pathak and M. B. Johnston, *Energy & Environmental Science*, 2014, **7**, 3061-3068.
10. P. P. Boix, S. Agarwala, T. M. Koh, N. Mathews and S. G. Mhaisalkar, *The Journal of Physical Chemistry Letters*, 2015.
11. V. Gonzalez-Pedro, E. J. Juarez-Perez, W.-S. Arsyad, E. M. Barea, F. Fabregat-Santiago, I. Mora-Sero and J. Bisquert, *Nano Lett*, 2014, **14**, 888-893.
12. M. Liu, M. B. Johnston and H. J. Snaith, *Nature*, 2013, **501**, 395-398.
13. O. Malinkiewicz, A. Yella, Y. H. Lee, G. M. Espallargas, M. Graetzel, M. K. Nazeeruddin and H. J. Bolink, *Nat Photon*, 2014, **8**, 128-132.
14. A. Kojima, M. Ikegami, K. Teshima and T. Miyasaka, *Chemistry Letters*, 2012, **41**, 397-399.
15. F. Deschler, M. Price, S. Pathak, L. E. Klintberg, D.-D. Jarausch, R. Higler, S. Hüttner, T. Leijtens, S. D. Stranks and H. J. Snaith, *The Journal of Physical Chemistry Letters*, 2014, **5**, 1421-1426.
16. Z.-K. Tan, R. S. Moggadam, M. L. Lai, P. Docampo, R. Higler, F. Deschler, M. Price, A. Sadhanala, L. M. Pazos and D. Credgington, *Nature nanotechnology*, 2014.
17. G. Xing, N. Mathews, S. S. Lim, N. Yantara, X. Liu, D. Sabba, M. Grätzel, S. Mhaisalkar and T. C. Sum, *Nat Mater*, 2014, **13**, 476-480.
18. A. Hinsch, W. Veurman, H. Brandt, K. Flarup Jensen and S. Mastroianni, *Chemphyschem*, 2014, **15**, 1076-1087.
19. A. Hinsch, presented in part at the WPVSEC, 2014, Kyoto, Korea.
20. F. Matteocci, S. Razza, F. Di Giacomo, S. Casaluci, G. Mincuzzi, T. M. Brown, A. D'Epifanio, S. Licoccia and A. Di Carlo, *Physical Chemistry Chemical Physics*, 2014, **16**, 3918-3923.
21. F. Matteocci, L. Cinà, F. Di Giacomo, S. Razza, A. L. Palma, A. Guidobaldi, A. D'Epifanio, S. Licoccia, T. M. Brown and A. Reale, *Progress in Photovoltaics: research and Applications*, 2014.
22. S. Razza, F. Di Giacomo, F. Matteocci, L. Cinà, A. L. Palma, S. Casaluci, P. Cameron, A. D'Epifanio, S. Licoccia and A. Reale, *Journal of Power Sources*, 2015, **277**, 286-291.
23. J. Seo, S. Park, Y. Chan Kim, N. J. Jeon, J. H. Noh, S. C. Yoon and S. I. Seok, *Energy & Environmental Science*, 2014, **7**, 2642-2646.
24. T. Fuyuki, H. Kondo, T. Yamazaki, Y. Takahashi and Y. Uraoka, *Applied Physics Letters*, 2005, **86**, 262108.
25. T. Trupke, R. Bardos, M. Schubert and W. Warta, *Applied Physics Letters*, 2006, **89**, 044107.
26. U. Rau, *Physical Review B*, 2007, **76**, 085303.
27. K. Tvingstedt, O. Malinkiewicz, A. Baumann, C. Deibel, H. J. Snaith, V. Dyakonov and H. J. Bolink, *Scientific reports*, 2014, **4**.
28. B. Michl, M. Padilla, I. Geisemeyer, S. T. Haag, F. Schindler, M. C. Schubert and W. Warta, 2014.
29. D. Hinken, C. Schinke, S. Herlufsen, A. Schmidt, K. Bothe and R. Brendel, *Review of Scientific Instruments*, 2011, **82**, 033706.
30. O. Breitenstein, J. Bauer, T. Trupke and R. A. Bardos, *Progress in Photovoltaics: research and Applications*, 2008, **16**, 325-330.
31. W. Shockley and H. J. Queisser, *Journal of Applied Physics*, 1961, **32**, 510-519.
32. W. Shockley and W. Read Jr, *Physical review*, 1952, **87**, 835.
33. R. N. Hall, *Physical review*, 1952, **87**, 387.
34. F. Bloch and P. Ross, *Physical review*, 1935, **47**, 884.
35. J. Nelson, *The physics of solar cells*, World Scientific, 2003.
36. W. Tress, N. Marinova, O. Inganäs, M. Nazeeruddin, S. M. Zakeeruddin and M. Graetzel, *Advanced Energy Materials*, 2014.
37. Y. Yamada, T. Nakamura, M. Endo, A. Wakamiya and Y. Kanemitsu, *J Am Chem Soc*, 2014, **136**, 11610-11613.
38. G. J. A. Wetzelaer, M. Scheepers, A. M. Sempere, C. Momblona, J. Ávila and H. J. Bolink, *Advanced Materials*, 2015.
39. S. D. Stranks, V. M. Burlakov, T. Leijtens, J. M. Ball, A. Gorieli and H. J. Snaith, *Physical Review Applied*, 2014, **2**, 034007.
40. X. Wu, M. T. Trinh, D. Niesner, H. Zhu, Z. Norman, J. S. Owen, O. Yaffe, B. J. Kudsich and X. Zhu, *J Am Chem Soc*, 2015.
41. H. J. Snaith, A. Abate, J. M. Ball, G. E. Eperon, T. Leijtens, N. K. Noel, S. D. Stranks, J. T.-W. Wang, K. Wojciechowski and W. Zhang, *The Journal of Physical Chemistry Letters*, 2014, **5**, 1511-1515.
42. W. Nie, H. Tsai, R. Asadpour, J.-C. Blancon, A. J. Neukirch, G. Gupta, J. J. Crochet, M. Chhowalla, S. Tretiak and M. A. Alam, *Science*, 2015, **347**, 522-525.
43. M. Saba, M. Cadelano, D. Marongiu, F. Chen, V. Sarritzu, N. Sestu, C. Figus, M. Aresti, R. Piras and A. G. Lehmann, *Nat Commun*, 2014, **5**.
44. J.-H. Im, I.-H. Jang, N. Pellet, M. Grätzel and N.-G. Park, *Nature nanotechnology*, 2014, **9**, 927-932.
45. A. Baldan, *Journal of Materials Science*, 2002, **37**, 2171-2202.
46. J. A. Christians, J. S. Manser and P. V. Kamat, *The Journal of Physical Chemistry Letters*, 2015, **6**, 852-857.
47. D. Hinken, K. Ramspeck, K. Bothe, B. Fischer and R. Brendel, *Applied Physics Letters*, 2007, **91**, 182104.
48. W. Tress, N. Marinova, O. Inganas, M. K. Nazeeruddin, S. M. Zakeeruddin and M. Graetzel, The role of the hole-transport layer in perovskite solar cells-reducing recombination and increasing absorption, 2014.
49. J. Reinhardt, M. Grein, C. Bühler, M. Schubert and U. Würfel, *Advanced Energy Materials*, 2014, **4**.
50. T. Leijtens, B. Lauber, G. E. Eperon, S. D. Stranks and H. J. Snaith, *The Journal of Physical Chemistry Letters*, 2014, **5**, 1096-1102.
51. T. Leijtens, S. D. Stranks, G. E. Eperon, R. Lindblad, E. M. Johansson, I. J. McPherson, H. Rensmo, J. M. Ball, M. M. Lee and H. J. Snaith, *ACS nano*, 2014, **8**, 7147-7155.
52. H. S. Kim, S. K. Kim, B. J. Kim, K.-S. Shin, M. G. Kumar, H. S. Jung, S.-W. Kim and N.-G. Park, *The Journal of Physical Chemistry Letters*, 2015.

ARTICLE

Journal Name

53. F. Zhu, L. Men, Y. Guo, Q. Zhu, U. Bhattacharjee, P. M. Goodwin, J. W. Petrich, E. A. Smith and J. Vela, *ACS nano*, 2015.
54. V. D'Innocenzo, A. R. Srimath Kandada, M. De Bastiani, M. Gandini and A. Petrozza, *J Am Chem Soc*, 2014.
55. Y. Shao, Z. Xiao, C. Bi, Y. Yuan and J. Huang, *Nature communications*, 2014, **5**.
56. M. Xiao, F. Huang, W. Huang, Y. Dkhissi, Y. Zhu, J. Etheridge, A. Gray-Weale, U. Bach, Y. B. Cheng and L. Spiccia, *Angewandte Chemie*, 2014, **126**, 10056-10061.
57. S. M. Vorpahl, S. D. Stranks, H. Nagaoka, G. E. Eperon, M. E. Ziffer, H. J. Snaith and D. S. Ginger, *Science*, 2015, **348**, 683-686.
58. D. Shi, V. Adinolfi, R. Comin, M. Yuan, E. Alarousu, A. Buin, Y. Chen, S. Hoogland, A. Rothenberger and K. Katsiev, *Science*, 2015, **347**, 519-522.
59. Q. Dong, Y. Fang, Y. Shao, P. Mulligan, J. Qiu, L. Cao and J. Huang, *Science*, 2015, **347**, 967-970.
60. L. Zheng, D. Zhang, Y. Ma, Z. Lu, Z. Chen, S. Wang, L. Xiao and Q. Gong, *Dalton Transactions*, 2015.
61. W.-J. Yin, T. Shi and Y. Yan, *Applied Physics Letters*, 2014, **104**, 063903.
62. P. Gundel, F. D. Heinz, M. C. Schubert, J. A. Giesecke and W. Warta, *Journal of Applied Physics*, 2010, **108**, 033705.